

# Approximate Bayesian inference for high-resolution spatial disaggregation using alternative data sources

Anis Pakrashi<sup>1,2</sup>, Arnab Hazra<sup>2</sup>,  
Sooraj M Raveendran<sup>3</sup>, and Krishnachandran Balakrishnan<sup>3</sup>

July 17, 2024

## Abstract

This paper addresses the challenge of obtaining precise demographic information at a fine-grained spatial level, a necessity for planning localized public services such as water distribution networks, or understanding local human impacts on the ecosystem. While population sizes are commonly available for large administrative areas, such as wards in India, practical applications often demand knowledge of population density at smaller spatial scales. We explore the integration of alternative data sources, specifically satellite-derived products, including land cover, land use, street density, building heights, vegetation coverage, and drainage density. Using a case study focused on Bangalore City, India, with a ward-level population dataset for 198 wards and satellite-derived sources covering 786,702 pixels at a resolution of  $30\text{m} \times 30\text{m}$ , we propose a semiparametric Bayesian spatial regression model for obtaining pixel-level population estimates. Given the high dimensionality of the problem, exact Bayesian inference is deemed impractical; we discuss an approximate Bayesian inference scheme based on the recently proposed max-and-smooth approach, a combination of Laplace approximation and Markov chain Monte Carlo. A simulation study validates the reasonable performance of our inferential approach. Mapping pixel-level estimates to the ward level demonstrates the effectiveness of our method in capturing the spatial distribution of population sizes. While our case study focuses on a demographic application, the methodology developed here readily applies to count-type spatial datasets from various scientific disciplines, where high-resolution alternative data sources are available.

**Keywords:** Alternative data sources; Approximate Bayesian inference; Spatial Gaussian process; Nonhomogeneous Poisson process; Semiparametric regression; Spatial disaggregation.

---

<sup>1</sup>Department of Statistics, Pennsylvania State University, University Park, Pennsylvania 16802, USA.  
E-mail: avp6357@psu.edu

<sup>2</sup>Department of Mathematics and Statistics, Indian Institute of Technology Kanpur, Kanpur 208016, India.  
E-mail: ahazra@iitk.ac.in

<sup>3</sup>Indian Institute of Human Settlements, Armane Nagar, Bengaluru, Karnataka 560080, India.  
E-mail: soorajmr@iihs.ac.in, krishna@mapsolve.ai

# 1 Introduction

Practical social problems often require analyzing data at finer-resolution spatial regions. The process of transitioning data from a higher (or finer) to a lower (or coarser) resolution is known as aggregation (Roquette et al., 2018; Paige et al., 2022). The delineation of boundaries frequently depends on the specific problem at hand, particularly observed in settings involving census data. However, utilizing statistical models based on aggregated data introduces certain natural disadvantages (Pollet et al., 2015). In various research domains such as forestry, agronomy, meteorology, public health, epidemiology, and soil science, information aggregation poses a significant challenge (van Beurden and Douven, 1999; Rudstrom et al., 2002). Finer-resolution unit information is often obscured due to aggregating data, making intricate trends invisible. The limitations associated with models for aggregated data drive the need for methodologies to recover the original (pixel-level) information from coarser resolution observations. This reverse process is referred to as spatial downscaling or disaggregation, with examples of applications provided by Mertens and Lambin (1997) and Muhling et al. (2018). Spatial disaggregation finds applications in hydrology (Alber and Piégay, 2011), census data (Monteiro et al., 2019), climate (Segond et al., 2007), agriculture (You et al., 2009), disease study (Arambepola et al., 2022), health (Utazi et al., 2019), and other fields.

Our study is motivated by a practical issue concerning data availability at larger spatial units, such as districts or wards in India, which commonly represent administrative boundaries. However, for applications requiring the subdivision of an entire city into distinct water-supply zones or understanding local human impacts on the ecosystem, ward-level data may not accurately depict the spatial distribution of the population, as noted by Sawicki (1973). Addressing this challenge involves spatial disaggregation, aiming to predict population figures at smaller spatial units, such as  $30\text{m} \times 30\text{m}$  pixels, which can then be aggregated based on specific requirements. Our study addresses the spatial disaggregation problem using a comprehensive dataset sourced from the Indian Institute of Human Settlements (IIHS), a national institution dedicated to the advancement and transformation of Indian cities and settlements.

The primary objective is to employ covariates at a resolution of  $30\text{m} \times 30\text{m}$  cells for disaggregating the population of Bangalore city, as documented by [Sudhira et al. \(2007\)](#). We focus particularly on Bruhat Bengaluru Mahanagara Palike (BBMP), the administrative body for the Bangalore metropolitan area, utilizing the 2011 Census data divided into 198 wards. Additional details about the setup and background can be found in [Balakrishnan \(2020\)](#). A possible solution is conducting high-resolution spatial disaggregation, drawing insights from relevant studies ([Earnest et al., 2010](#); [Utazi et al., 2019](#); [Sadik et al., 2020](#)). A homogeneous Poisson Process assumption is clearly unsuitable. A spatially-varying intensity function of the underlying nonhomogeneous Poisson process can be well estimated using a semiparametric approach or a spline-based method. A Gaussian process approximation to the likelihood is also effective due to the large population sizes in each ward. Additional applications of the Gaussian process in spatial analysis are in [Tapia et al. \(2016\)](#) and [Bullock et al. \(2023\)](#).

Alternative data sources are indispensable in statistical research, particularly in spatial data studies, due to their capacity to complement conventional datasets, address data gaps, enhance precision, facilitate exploration of novel research questions, and increase robustness through data integration. These alternative sources, encompassing remote sensing data, social media geotagged information, and crowd-sourced data, offer distinct advantages including real-time insights, finer resolution, accessibility to remote regions, and the facilitation of novel methodologies and research domains ([Foulkes and Newbold, 2008](#); [Golder and Macy, 2011](#); [Wulder et al., 2012](#); [Machado et al., 2021](#); [de Oliveira et al., 2023](#)). By harnessing the diversity of these data sources, researchers can surmount the limitations inherent in traditional datasets, thus revealing deeper insights into multifaceted phenomena spanning various disciplines. In our study, data for several important predictors of population density were collected using satellite imaging, deep learning, and computer vision techniques, resulting in datasets with high-resolution information essential for estimating responses at finer spatial resolutions.

Different approaches in the past have led to a vast repository of disaggregation approaches, although each has its own limitations. [Mertens and Lambin \(1997\)](#) discuss an application to

deforestation modeling using traditional spatial modeling techniques. [Muhling et al. \(2018\)](#) explain disaggregation approaches like bias-corrected quantile mapping (BCQM), change factor quantile mapping (CFQM), equidistant quantile mapping (EDQM), and the cumulative distribution function transform (CDFt) on various computer models for water temperature and salinity, called general circulation models. [Utazi et al. \(2019\)](#) develop a methodology for high-resolution mapping of vaccination coverage using a binomial spatial regression model with a logit link and a combination of covariate data and random effects modeling two levels of spatial autocorrelation in the linear predictor. The authors build their proposed Bayesian model using a stochastic partial differential equation (SPDE) approach of [Lindgren et al. \(2011\)](#) and the computation involves the integrated nested Laplace approximation (INLA) approach of [Rue et al. \(2009\)](#). [Nandi et al. \(2023\)](#) design an R package `disaggregation` to implement spatial disaggregation; they also use SPDE, an approximation to dense Gaussian processes (GPs) using Gaussian Markov random fields that allow sparse precision matrices. The approximation errors are unavoidable and depend on the mesh construction and the true range of the underlying GP which is generally unknown for real datasets ([Hazra et al., 2021](#); [Cisneros et al., 2023](#)). Thus, a true dense GP, if computationally feasible, is preferred. Besides, a very high-resolution ( $30\text{m} \times 30\text{m}$ , for example) spatial disaggregation using these above approaches can be highly computationally challenging.

Bayesian hierarchical models have proven instrumental in simplifying intricate Bayesian problems, effectively addressing problems characterized by unknown or complex joint distributions by breaking them down into multilevel structures with priors and hyperpriors at various levels ([Schmid and Brown, 2000](#)). By accommodating multiple sources of variability, hierarchical models provide consistent and accurate estimates, demonstrating broad applicability across various real-life domains, including medical sciences ([Yang et al., 2022](#); [Li et al., 2023](#)), climatology and geosciences ([Berliner et al., 2000](#); [Wainwright et al., 2016](#)), as well as in ecology ([Wikle, 2003](#); [Ponciano et al., 2009](#)). In spatial disaggregation or downscaling problems, these models have been found particularly useful ([Anjoy et al., 2019](#); [Shiferaw, 2023](#)).



Using a posterior predictive approach, fine-scale information can be obtained by employing a multiple-layer Bayesian structure, each corresponding to an aspect at a coarser resolution (Tassone et al., 2010; Tasic et al., 2016; Irekponor et al., 2022; Murphy et al., 2023). Bayesian latent Gaussian models are Bayesian hierarchical models that assign Gaussian prior densities to the latent parameters and they are widely used in different scientific disciplines (Hazra et al., 2023; Hrafinkelsson and Bakka, 2023).

Closed-form expressions of the posterior distributions of the model parameters exist mostly in naive examples and the posteriors usually involve high-dimensional integrals. Techniques such as variational inference, Markov chain Monte Carlo (MCMC), and sequential Monte Carlo (SMC) provide avenues for approximating posterior distributions, circumventing the need for explicit computation of high-dimensional integrals (Brooks et al., 2011). These methods find broad application across diverse fields, including machine learning, computational biology, econometrics, and computational neuroscience, facilitating probabilistic modeling, uncertainty quantification, parameter estimation, and forecasting (Harva et al., 2008; Martino et al., 2011; Stumpf, 2014). For Bayesian latent Gaussian spatial models, standard MCMC algorithms are commonly used (Hazra et al., 2021) and INLA is a common deterministic computation-based algorithm (Utazi et al., 2019). In case the likelihood and prior both are Gaussian, the posterior is also Gaussian due to conjugacy, and several computationally attractive tools are available in the literature for sampling from high-dimensional Gaussian posteriors (Gelfand and Schliep, 2016). However, in the likelihood is non-Gaussian, such a conjugacy does not hold; using a random-walk Metropolis-Hastings algorithm or its advanced variants for updating parameters is common here (Yadav et al., 2023). When the dimension of the parameter vector is extremely high (786,702 in our case), existing exact computing tools are not feasible and an approximate Bayesian inference is a possible solution here. A recently proposed Max-and-Smooth approach (Hrafinkelsson et al., 2021) approximates the non-Gaussian likelihood using a Gaussian likelihood via Laplace approximation and subsequently, for a Gaussian prior, the conjugacy of the prior, and the approximated likelihood is used for updating high-dimensional

parameter vectors using INLA (Jóhannesson et al., 2022) or MCMC (Hazra et al., 2023).

We assume that the coordinates of individuals follow a non-homogeneous Poisson point process and thus model the ward-specific population counts of Bangalore using independent Poisson distributions, where we model the underlying intensity function using a Gaussian process without any sparsity-based (SPDE, for example) or low-rank approximation (Wikle, 2003). Following a Laplace approximation of the ward-level Poisson likelihood, we explore the Max-and-Smooth approach, where the approximate full conditional posterior of the intensity function follows a Gaussian process. Subsequently, we explore a Gibbs sampling algorithm for drawing posterior samples without involving Metropolis-Hastings steps. We discuss a careful choice of the prior distribution for the spatial range parameter of the Poisson intensity function that makes the computation and storage feasible. Further, while drawing exact samples from the underlying 786,702-dimensional multivariate normal full conditional posterior distribution for the vector of Poisson intensity parameters is infeasible, at least on a standard workstation, we discuss Monte Carlo estimates of the pixel-wise posterior means and posterior standard deviations without performing such high-dimensional draws. Implementation and architecture of coding (written in R and provided in the supplementary material) is crucial here to avoid memory and storage exhaustion on a standard workstation, and we also discuss these issues. In a simulation study and the Bangalore population data application, we compare our method with a non-spatial Gaussian process prior for the Poisson intensity function and with a standard Bayesian generalized linear model approach.

This paper is structured as follows: Section 2 offers a succinct overview of the Bangalore population dataset, encompassing the response variable, predictors, and potential relationships between the response and predictors. Section 3 elaborates on the methodology, model properties, and a practical approximate Bayesian computational scheme. The outcomes of a simulation study are presented in Section 4. Moving to Section 5, the proposed disaggregation method is applied to the Bangalore population dataset, with a detailed presentation of results and comparisons. Finally, Section 6 provides concluding remarks.

## 2 Bangalore population data and exploratory analysis

Our primary objective is to utilize alternative data sources as predictors, available at a resolution of  $30\text{m} \times 30\text{m}$  at 786,702 pixels, for disaggregating the ward-level population data for Bruhat Bengaluru Mahanagara Palike (BBMP), the administrative body overseeing the Bangalore metropolitan area (henceforth, Bangalore). The dataset includes ward-level information from the 2011 Census for BBMP, encompassing 198 wards. For each pixel, we have information about the specific ward that contains it, and thus we can easily map from 786,702 pixels to 198 wards and calculate the number of pixels within each ward.

The left panel of Figure 1 represents the ward-level population sizes of Bangalore. In contrast, the right panel shows empirical log-intensities (the natural logarithm of the population values divided by the respective numbers of pixels within wards). The empirical log-intensities essentially capture the logarithm of population densities across different wards. While the central region of Bangalore appears to have lower population values than the wards near the periphery, the areas of the wards in the central region are smaller. Notably, the central region, being the Information Technology hub, also known as the Silicon Valley of India, exhibits higher densities, while the suburbs near the periphery are sparsely populated. Given that the log-densities vary across different parts of the city, it is prudent to model the data using a non-homogeneous Poisson process that accommodates spatially-varying intensities across the spatial domain. This approach allows for a more realistic and nuanced modeling of the population distribution in Bangalore.

In addition to population data, we consider various predictors, including land cover categories (1: Built-up; 2: Vegetation; 3: Water; 4: Vacant), a binary indicator of land use (1: Residential; 0: Non-residential), street density within each pixel, building height (in meters) estimated from stereo imagery, and sub-pixel ( $5\text{m} \times 5\text{m}$ ) indicators denoting built-up areas, vegetation cover, or vacant land. Furthermore, we include a continuous measure of drainage network density within each pixel. We present the spatial maps of these predictors in Figure 2, which are available at the pixel level ( $30\text{m} \times 30\text{m}$ ). We observe significant variation in

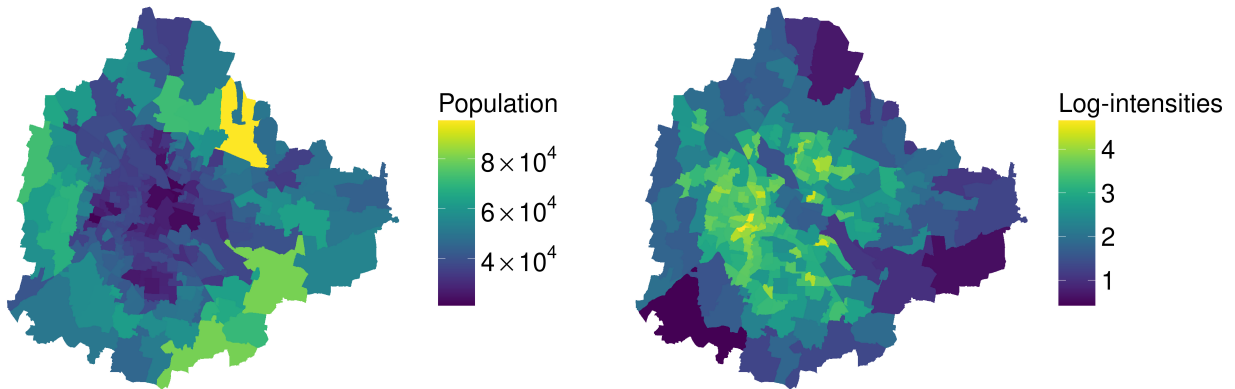


Figure 1: Left: Ward-level population sizes in Bangalore city area, Right: Empirical log-intensities in Bangalore.

the values or levels of the covariates across different regions of Bangalore, except drainage density. For instance, the central portion of the city exhibits more built-up areas, higher proportions of residential areas, taller buildings, and less vegetation compared to the suburbs. The drainage density, however, displays a unique pattern, with higher values consistently aligned with drainage lines throughout the city, irrespective of the region. This detailed analysis of covariates provides a comprehensive understanding of the diverse spatial characteristics influencing spatial population distribution and urban dynamics in Bangalore.

We further explore the linear relationship between the response and predictors. While a nonlinear relationship is more robust and flexible, we have only 198 observations from the response variable, and hence, a linearity assumption provides parsimony. Considering a Poisson model for the data layer, a natural choice is exploring the linear relationships of the predictors with empirical log-intensities instead of actual population sizes. We present the scatterplots in Figure 3, illustrating the relationship between the log-intensities and predictors at the ward level. The figures suggest that assuming linearity is reasonable. Here, land cover and vegetation count exhibit a negative linear relationship with the log-intensities, while the other predictors demonstrate a positive relationship. These plots justify using the available predictors for modeling the spatially-varying intensity of the Poisson point process model.

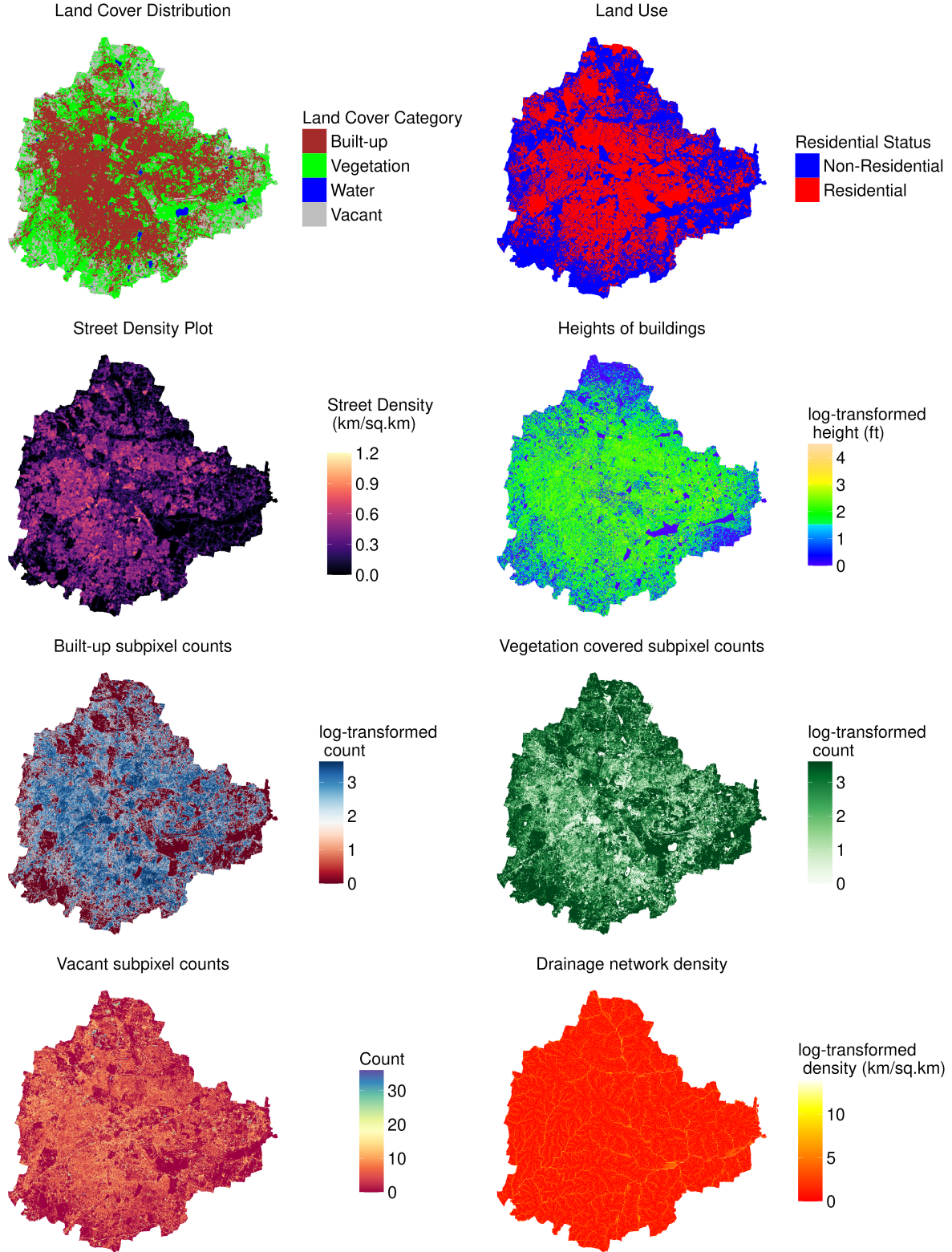


Figure 2: Spatial maps of the satellite-derived alternative data sources. Here we transform some variables using the transformation  $f(x) = \log(1 + x)$ , as otherwise, certain crucial patterns are not clearly visible. In such cases, we use the term ‘log-transformed’.

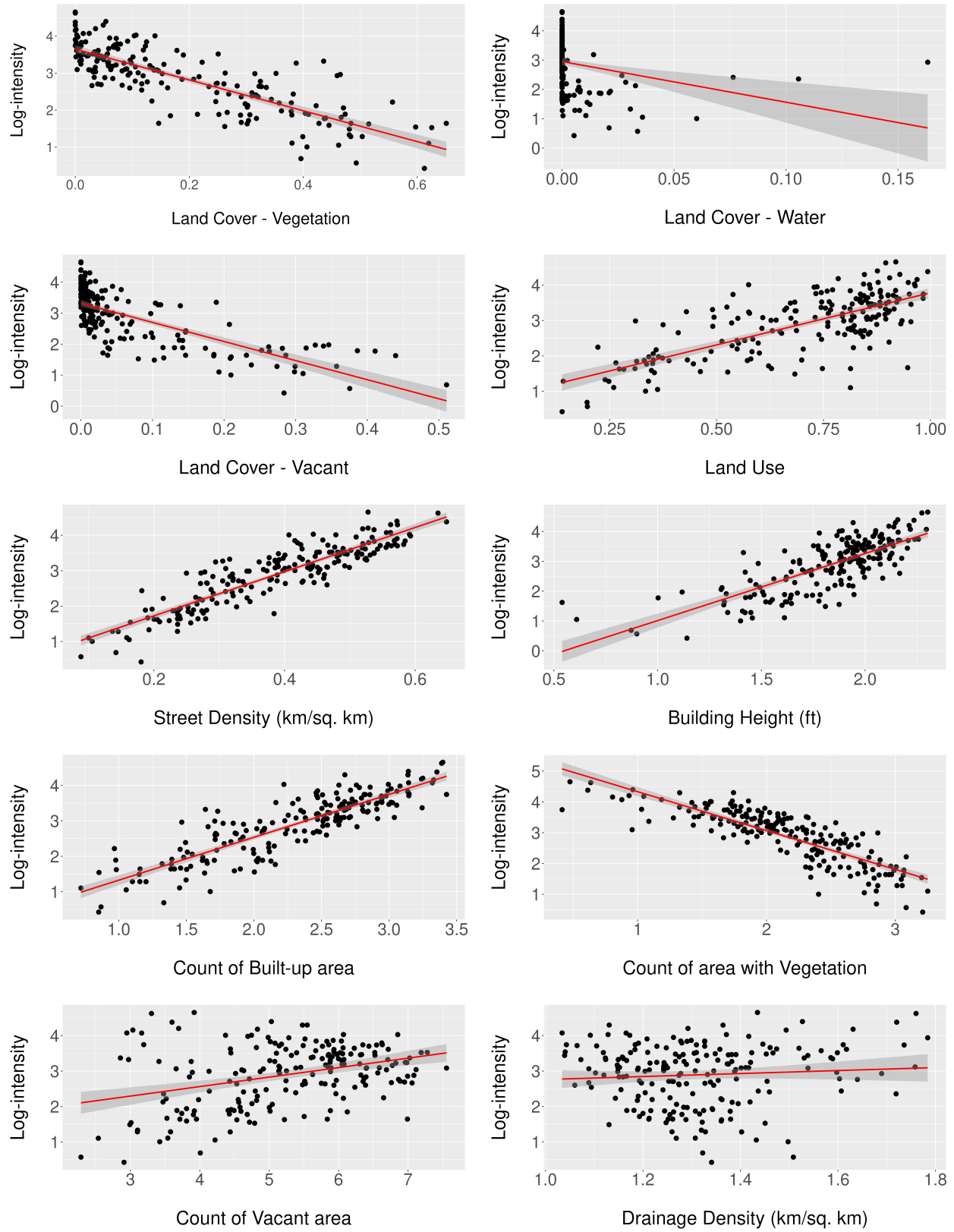


Figure 3: Relationships between log-intensities of population and transformed covariates in the dataset. The transformations considered here are the same as in Figure 2.



A common approach for exploring the linear relationship between the predictors and the count-type variables is the generalized linear model, specifically, a Poisson regression model with a log link. Here, for  $L = 198$  wards, using the `glm` function in R, we fit the model  $Y_i \stackrel{\text{Indep}}{\sim} \text{Poisson}(|\mathcal{A}_i|\lambda_i)$ , where  $\log(\lambda_i) = \tilde{\mathbf{x}}_i^T \boldsymbol{\beta}$  for  $i \in \{1, 2, \dots, L\}$ ,  $|\mathcal{A}_i|$  denotes the number of  $30\text{m} \times 30\text{m}$  pixels within the  $i$ -th ward,  $\tilde{\mathbf{x}}_i$  denotes the vector of predictors in Figure 3, and  $\boldsymbol{\beta}$  denotes the vector of regression coefficients. We present the results in Table 1. Except for the predictor ‘Land cover-Vegetation’, all others exhibit a significant linear relationship indicating their importance in modeling the spatial variation of the intensity function of the underlying Poisson point model in a proper Bayesian modeling framework.

Table 1: Parameter estimates, corresponding standard errors,  $z$ -values, and  $p$ -values of fitting a simple Poisson regression model to the ward-specific population sizes.

Predictor	Estimate	Std. Error	$z$ -value	$p$ -value
Intercept	2.0037	0.00046	4314.8457	<0.0001
Land cover-Vegetation	-0.0016	0.00303	-0.5334	0.5938
Land cover-Water	-0.2472	0.00285	-86.7009	<0.0001
Land cover-Vacant	-0.3773	0.00219	-172.3996	<0.0001
Land Use	0.2616	0.00139	187.8546	<0.0001
Street Density	0.6769	0.00129	524.6790	<0.0001
Building Height	0.0162	0.00194	8.3462	<0.0001
Builtup Count	-0.2661	0.00360	-73.8608	<0.0001
Vegetation Count	-0.8245	0.00240	-343.5274	<0.0001
Vacant Count	0.2426	0.00260	93.3627	<0.0001
Drainage Density	0.0975	0.00462	21.1017	<0.0001

While the available predictor information helps in analyzing the spatial variation, the unexplained variability needs to be modeled in a spatially-dependent framework for the Poisson intensity function. In our exploratory analysis, the empirical log-intensity is a proxy for the intensity function of the Poisson point process. We thus regress the empirical log-intensity based on the predictors shown in Figure 3 using linear regression and explore the semivariance of the residuals across the wards. Here we consider the Euclidean distance between the centroids of the wards. The semivariance of the residual process at distance  $h$  is

$$\gamma(h) = \frac{1}{2|N(h)|} \sum_{N(h)} (Z_i - Z_j)^2,$$

where  $N(h)$  is the set of all pairwise distances  $(i, j)$  with  $i - j = h$ ,  $|N(h)|$  being the number of unique pairs in  $N(h)$ , and  $Z_i$  and  $Z_j$  are the values of the residuals of the log-intensities at wards  $i$  and  $j$ . We present the empirical semivariance in Figure 4, where the presence of spatial correlation is clear. Further, we fit an exponential covariance kernel with parameters estimated using the function `fit.variogram` function in R. The corresponding fitted semivariance is presented using a solid line in Figure 4, which indicates that an exponential covariance kernel provides a reasonable fit to the spatial dependence structure of the log-intensity.

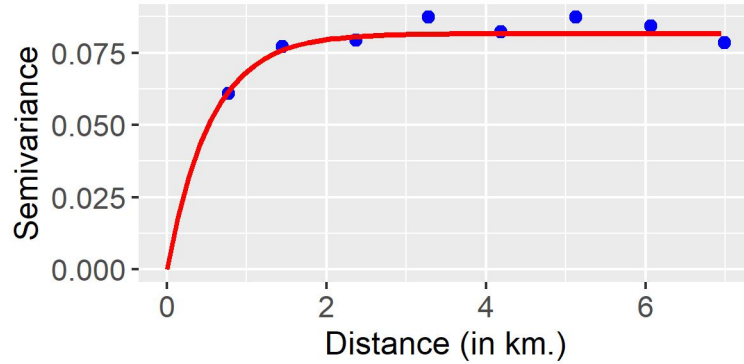


Figure 4: Empirical (dots) and fitted (line) semivariance of empirical log-intensity of population after removing effects of covariates. Here the fitted line is based on an exponential covariance kernel with parameters estimated using the function `fit.variogram` function in R.

## 3 Methodology

### 3.1 Spatial disaggregation model

Suppose  $Y_i, i = 1, \dots, L$  denote the population sizes for  $L = 198$  wards in Bangalore. Each ward comprises several  $30\text{m} \times 30\text{m}$  pixels, with the number of pixels ranging between 358 and 33035, and in total, there are  $P = 786,702$  pixels. We further consider the area of a pixel as a single unit. Let the spatial domains for the  $L$  wards be denoted by  $\mathcal{A}_i \subset \mathbb{R}^2, i = 1, \dots, L$  and the entire study domain is  $\mathcal{A} = \sqcup_{i=1}^L \mathcal{A}_i$ . Here,  $\mathcal{A}_i \cap \mathcal{A}_j = \emptyset$  for  $i \neq j$ . Let the vector of predictors at a spatial coordinate  $\mathbf{s}$  be denoted by  $\mathbf{X}(\mathbf{s})$  and its spatial average within the  $i$ -th ward is  $\widetilde{\mathbf{X}}_i = |\mathcal{A}_i|^{-1} \int_{\mathcal{A}_i} \mathbf{X}(\mathbf{s}) d\mathbf{s}$ , where  $|\mathcal{A}_i|$  denotes the area of the  $i$ -th ward. While the predictor information is available at pixel levels, let the vector of predictors for the  $j$ -th pixel,



with centroid  $\mathbf{s}_j$ , be denoted by  $\mathbf{X}(\mathbf{s}_j)$ .

We model the coordinates of the people using a non-homogeneous Poisson process (NHPP), and thus, for  $\lambda_i$  denoting the average intensity within a pixel, we have

$$Y_i \sim \text{Poisson}(|\mathcal{A}_i|\lambda_i). \quad (1)$$

Given the  $\lambda_i$ 's are always positive and the most natural way of modeling spatial dependence is using Gaussian processes (GPs, [Gelfand and Schliep, 2016](#)), we model the intensity function in the log scale as

$$\lambda^*(\mathbf{s}) \equiv \log[\lambda(\mathbf{s})] = \mathbf{X}(\mathbf{s})^T \boldsymbol{\beta} + \eta(\mathbf{s}), \quad (2)$$

where  $\eta(\cdot)$  is a zero-mean GP with exponential covariance kernel defined over  $\mathcal{A}$ . We denote it by  $\eta(\cdot) \sim \text{GP}(0, K(\cdot, \cdot))$ , where  $K(\mathbf{s}, \mathbf{s}') = \sigma^2 \exp\{-d(\mathbf{s}, \mathbf{s}')/\phi\}$ . Here,  $\sigma^2$  and  $\phi$  are marginal variance and spatial range parameter of the underlying GP, respectively. Given that  $\mathcal{A}$  is a small geographical domain, we consider  $d(\mathbf{s}, \mathbf{s}') = \|\mathbf{s} - \mathbf{s}'\|$ , the Euclidean distance, which would be approximately equivalent with geodesic distance. Overall,  $\lambda^*(\cdot) \sim \text{GP}(\mathbf{X}(\mathbf{s})^T \boldsymbol{\beta}, K(\cdot, \cdot))$  with  $K(\mathbf{s}, \mathbf{s}') = \sigma^2 \exp\{-\|\mathbf{s} - \mathbf{s}'\|/\phi\}$ .

The link between (1) and (2) follows from the equation

$$\lambda_i^* \equiv \log[\lambda_i] = |\mathcal{A}_i|^{-1} \int_{\mathcal{A}_i} \lambda^*(\mathbf{s}) d\mathbf{s} \equiv \log[\lambda(\mathbf{s})] = \widetilde{\mathbf{X}}_i^T \boldsymbol{\beta} + |\mathcal{A}_i|^{-1} \int_{\mathcal{A}_i} \eta(\mathbf{s}) d\mathbf{s}. \quad (3)$$

Here,  $\lambda_i^*$  follows a univariate normal distribution; this result follows directly from the fact that a linear combination of a multivariate normal vector is normal and integration is a linear operator. Similarly, the vector  $\boldsymbol{\lambda}^* = (\lambda_1^*, \dots, \lambda_L^*)'$  follows a multivariate normal distribution. The mean, variance, and covariances for  $\lambda_i, i \in \{1, \dots, L\}$  are given by

$$\begin{aligned} \mathbb{E}(\lambda_i^*) &= |\mathcal{A}_i|^{-1} \int_{\mathcal{A}_i} [\mathbf{X}(\mathbf{s})^T \boldsymbol{\beta}] d\mathbf{s} = \left[ |\mathcal{A}_i|^{-1} \int_{\mathcal{A}_i} \mathbf{X}(\mathbf{s}) d\mathbf{s} \right]^T \boldsymbol{\beta} = \widetilde{\mathbf{X}}_i^T \boldsymbol{\beta}, \\ \text{Var}(\lambda_i^*) &= \sigma^2 |\mathcal{A}_i|^{-2} \int_{\mathcal{A}_i} \int_{\mathcal{A}_i} \exp\{-\|\mathbf{s} - \mathbf{s}'\|/\phi\} d\mathbf{s} d\mathbf{s}', \\ \text{Cov}(\lambda_i^*, \lambda_j^*) &= \sigma^2 |\mathcal{A}_i|^{-1} |\mathcal{A}_j|^{-1} \int_{\mathcal{A}_i} \int_{\mathcal{A}_j} \exp\{-\|\mathbf{s} - \mathbf{s}'\|/\phi\} d\mathbf{s} d\mathbf{s}'. \end{aligned} \quad (4)$$

A natural proxy for  $\widetilde{\mathbf{X}}_i$  is the average of  $\mathbf{X}(\mathbf{s}_j)$ 's with  $\mathbf{s}_j \in \mathcal{A}_i$  and we calculate  $\widetilde{\mathbf{X}}_i$  in the same way for further computations. Similarly, because we consider the area of a pixel as a unit, the natural proxy for  $|\mathcal{A}_i|$  is the number of pixels within the  $i$ -th ward. The term  $\text{Var}(\lambda_i^*)$  is enumerated by  $\sigma^2 |\mathcal{A}_i|^{-2} \sum_{\mathbf{s}_j \in \mathcal{A}_i} \sum_{\mathbf{s}_{j'} \in \mathcal{A}_i} \exp\{-\|\mathbf{s}_j - \mathbf{s}_{j'}\|/\phi\}$ . Similarly, the term  $\text{Cov}(\lambda_i^*, \lambda_j^*)$  is enumerated by  $\sigma^2 |\mathcal{A}_i|^{-1} |\mathcal{A}_j|^{-1} \sum_{\mathbf{s}_l \in \mathcal{A}_i} \sum_{\mathbf{s}_{l'} \in \mathcal{A}_j} \exp\{-\|\mathbf{s}_l - \mathbf{s}_{l'}\|/\phi\}$ . Overall, given the parameters  $\boldsymbol{\beta}$ ,  $\sigma^2$ , and  $\phi$ , we write  $\boldsymbol{\lambda}^* | \boldsymbol{\beta}, \sigma^2, \phi \sim \text{N}_L(\widetilde{\mathbf{X}}\boldsymbol{\beta}, \sigma^2 \boldsymbol{\Sigma}_{00}^{(\phi)})$ , where  $\widetilde{\mathbf{X}}$  is obtained by stacking  $\widetilde{\mathbf{X}}_i$ 's and the  $(i, j)$ -th element of  $\boldsymbol{\Sigma}_{00}^{(\phi)}$  equals  $|\mathcal{A}_i|^{-1} |\mathcal{A}_j|^{-1} \sum_{\mathbf{s}_l \in \mathcal{A}_i} \sum_{\mathbf{s}_{l'} \in \mathcal{A}_j} \exp\{-\|\mathbf{s}_l - \mathbf{s}_{l'}\|/\phi\}$ .

Our main aim in this analysis is to draw inferences about  $\lambda^*(\mathbf{s}_j)$  for all  $\mathbf{s}_j \in \mathcal{A}_i$  for  $i = 1, \dots, L$ , i.e., the vector of log-intensities at  $P = 786,702$  pixels. Stacking all  $\lambda^*(\mathbf{s}_j)$ 's into a vector  $\boldsymbol{\lambda}_p^*$ , the joint distribution of  $\boldsymbol{\lambda}_p^*$  would be a  $P$ -dimensional multivariate normal distribution with marginal means  $\text{E}[\lambda^*(\mathbf{s}_j)] = \mathbf{X}(\mathbf{s}_j)^T \boldsymbol{\beta}$ , marginal variances  $\text{Var}[\lambda^*(\mathbf{s}_j)] = \sigma^2$ , and covariances  $\text{Cov}[\lambda^*(\mathbf{s}_j), \lambda^*(\mathbf{s}_{j'})] = \sigma^2 \exp\{-\|\mathbf{s}_j - \mathbf{s}_{j'}\|/\phi\}$ . Overall, we denote the joint distribution of  $\boldsymbol{\lambda}_p^*$  by  $\boldsymbol{\lambda}_p^* | \boldsymbol{\beta}, \sigma^2, \phi \sim \text{N}_P(\mathbf{X}\boldsymbol{\beta}, \sigma^2 \boldsymbol{\Sigma}_{pp}^{(\phi)})$ , where  $\mathbf{X}$  is obtained by stacking  $\mathbf{X}(\mathbf{s}_j)$ 's across rows and  $\boldsymbol{\Sigma}_{pp}^{(\phi)}$  is obtained by filling its diagonal elements with ones and off-diagonal elements with  $\exp\{-\|\mathbf{s}_j - \mathbf{s}_{j'}\|/\phi\}$  terms. Regarding joint distributions of  $\boldsymbol{\lambda}_p^*$  and  $\boldsymbol{\lambda}^*$ , the vector  $(\boldsymbol{\lambda}_p^{*T}, \boldsymbol{\lambda}^{*T})^T$  exhibit a joint normal distribution with a mean vector of  $(\mathbf{X}^T | \widetilde{\mathbf{X}}^T)^T \boldsymbol{\beta}$  and a dispersion matrix of  $\sigma^2 [(\boldsymbol{\Sigma}_{pp}^{(\phi)} \quad \boldsymbol{\Sigma}_{p0}^{(\phi)}), (\boldsymbol{\Sigma}_{0p}^{(\phi)} \quad \boldsymbol{\Sigma}_{00}^{(\phi)})]$ . The elements of the cross-covariance matrix  $\sigma^2 \boldsymbol{\Sigma}_{p0}^{(\phi)}$  are filled with terms  $\text{Cov}[\lambda^*(\mathbf{s}_j), \lambda_i^*] = |\mathcal{A}_i|^{-1} \sum_{\mathbf{s}_l \in \mathcal{A}_i} \exp\{-\|\mathbf{s}_j - \mathbf{s}_l\|/\phi\}$ . Thus,

$$\boldsymbol{\lambda}_p^* | \boldsymbol{\lambda}^*, \boldsymbol{\beta}, \sigma^2, \phi \sim \text{N}_P \left( \mathbf{X}\boldsymbol{\beta} + \boldsymbol{\Sigma}_{p0}^{(\phi)} \boldsymbol{\Sigma}_{00}^{(\phi)-1} \left( \boldsymbol{\lambda}^* - \widetilde{\mathbf{X}}\boldsymbol{\beta} \right), \sigma^2 \left( \boldsymbol{\Sigma}_{pp}^{(\phi)} - \boldsymbol{\Sigma}_{p0}^{(\phi)} \boldsymbol{\Sigma}_{00}^{(\phi)-1} \boldsymbol{\Sigma}_{0p}^{(\phi)} \right) \right). \quad (5)$$

We further specify hyperpriors for  $\boldsymbol{\beta}$ ,  $\sigma^2$ , and  $\phi$ . Assuming there are  $m$  predictors available ( $m = 10$  in our data application) except the intercept, we assume  $\boldsymbol{\beta} \sim \text{N}_{m+1}(\mathbf{0}, 100^2 I_{m+1})$  which is a weakly-informative conjugate prior. By similar logic, for  $\sigma^2$ , we choose the hyperprior  $\sigma^2 \sim \text{Inverse-Gamma}(0.01, 0.01)$ . The choice of hyperprior for  $\phi$  is crucial as the computational burden heavily depends on the hyperprior selection. Based on evidence from the exploratory analysis, we notice that the range parameter is likely to be between 75 meters and 575 meters, and considering 30m (distance between two first-order neighboring pixels) as a unit,  $\phi$  is likely to vary between 2.5 and 17.5. We then choose the prior

$\phi \sim \text{Discrete-Uniform}\{2.5, 2.75, 3, \dots, 17.5\}$ . Although we guess the possible range of values of  $\phi$  based on exploratory analysis, it is not an empirical Bayes approach. Ideally, the lower limit and upper limit can be tuned to allow a wider range of values, along with a finer grid of values, but the computation can be infeasible; we discuss further details about the computational bottleneck in Section 3.3.

Finally, we write the overall hierarchical Bayesian model as

$$\begin{aligned}
Y_i | \lambda_i^* &\stackrel{\text{Indep}}{\sim} \text{Poisson}(|\mathcal{A}_i| \exp\{\lambda_i^*\}), \\
\boldsymbol{\lambda}^* = (\lambda_1^*, \dots, \lambda_L^*)' | \boldsymbol{\beta}, \sigma^2, \phi &\sim N_L(\widetilde{\mathbf{X}}\boldsymbol{\beta}, \sigma^2 \boldsymbol{\Sigma}_{00}^{(\phi)}), \\
\boldsymbol{\lambda}_p^* | \boldsymbol{\lambda}^*, \boldsymbol{\beta}, \sigma^2, \phi &\sim N_P(\mathbf{X}\boldsymbol{\beta} + \boldsymbol{\Sigma}_{p0}^{(\phi)} \boldsymbol{\Sigma}_{00}^{(\phi)-1} (\boldsymbol{\lambda}^* - \widetilde{\mathbf{X}}\boldsymbol{\beta}), \sigma^2 (\boldsymbol{\Sigma}_{pp}^{(\phi)} - \boldsymbol{\Sigma}_{p0}^{(\phi)} \boldsymbol{\Sigma}_{00}^{(\phi)-1} \boldsymbol{\Sigma}_{0p}^{(\phi)})) \\
\boldsymbol{\beta} &\sim N_{m+1}(\mathbf{0}, 100^2 \mathbf{I}_{m+1}), \\
\sigma^2 &\sim \text{Inverse-Gamma}(0.01, 0.01), \\
\phi &\sim \text{Discrete-Uniform}\{2.5, 2.75, 3, \dots, 17.5\}.
\end{aligned} \tag{6}$$

### 3.2 Model properties

After integrating out the latent Gaussian process  $\lambda^*(\cdot)$ , the marginal mean, variance, and covariances of  $Y_i, i \in \{1, \dots, L\}$  are as follows.

$$\begin{aligned}
E(Y_i) &= |\mathcal{A}_i| \cdot \exp\{\widetilde{\mathbf{X}}_i^T \boldsymbol{\beta} + \psi\}, \\
\text{Var}(Y_i) &= |\mathcal{A}_i|^2 \cdot \exp\left[2\widetilde{\mathbf{X}}_i^T \boldsymbol{\beta} + 2\psi\right] (\exp\{\psi\} - 1) + |\mathcal{A}_i| \cdot \exp\{\widetilde{\mathbf{X}}_i^T \boldsymbol{\beta} + \psi\}, \\
&\quad \text{where } \psi = \frac{\sigma^2}{2} |\mathcal{A}_i|^{-2} \int_{\mathcal{A}_i} \int_{\mathcal{A}_i} \exp\{-d(\mathbf{s}, \mathbf{s}')/\phi\} d\mathbf{s} d\mathbf{s}', \\
\text{Cov}(Y_i, Y_j) &= E(Y_i Y_j) - E(Y_i) \cdot E(Y_j) \neq 0, \text{ as } \text{Cov}(\lambda_i^*, \lambda_j^*) \neq 0.
\end{aligned} \tag{7}$$

Keeping other parameters fixed, the regression term  $\widetilde{\mathbf{X}}_i^T \boldsymbol{\beta}$  appears both in the first and second order moments of  $Y_i$ 's and its larger value implies larger mean and variance terms. Similarly, increasing  $\sigma^2$  and/or  $\phi$  implies larger means. A higher value of  $\phi$  indicates increased spatial association and thus increased spatial aggregates on an average. A Poisson distribution with a fixed intensity parameter is equidispersed and it is always overdispersed for a random intensity parameter. Thus, we also have  $\text{Var}(Y_i) > E(Y_i)$  for  $i = 1, \dots, L$ .

### 3.3 Computation

The first major challenge lies in the computation of the  $\Sigma_{00}^{(\phi)}$  matrices and both computation and storage of the  $\Sigma_{p0}^{(\phi)}$  matrices. For each value of  $\phi$ , we need to calculate the  $198 \times 198$  dimensional symmetric matrix  $\Sigma_{00}^{(\phi)}$  and thus it involves calculating 19,701 unique pair of elements. As mentioned in Section 3.1, the  $(i, j)$ -th element of  $\Sigma_{00}^{(\phi)}$  is calculated by  $|\mathcal{A}_i|^{-1}|\mathcal{A}_j|^{-1} \sum_{\mathbf{s}_l \in \mathcal{A}_i} \sum_{\mathbf{s}_{l'} \in \mathcal{A}_j} \exp\{-\|\mathbf{s}_l - \mathbf{s}_{l'}\|/\phi\}$ , where the number of pixels varies between 358 and 33035 across wards and thus involves huge computational burden. Given the computation for 19,701 pairs of elements can be done in parallel, we perform parallel computing across 20 cores of a workstation equipped with AMD Ryzen 9 processor with 64 GB DDR4 RAM and 4 TB storage, and the overall time for calculating  $\Sigma_{00}^{(\phi)}$  is approximately 30 minutes. Each  $\Sigma_{00}^{(\phi)}$  matrix required a storage space of 288 KB. We use the same computational and storage facilities for subsequent calculations. Further, we again calculate the elements of the  $786,702 \times 198$ -dimensional  $\Sigma_{p0}^{(\phi)}$  matrix in parallel across 20 cores, and the computation time is approximately 36 minutes. Besides, it requires a storage cost of 1.2 GB.

Overall, if the parameter space of  $\phi$  involves  $n_\phi$  elements, the total computation time is approximately  $66 \times n_\phi$  minutes, and it requires a storage cost of approximately  $1.2 \times n_\phi$  GB. Naturally, a continuous prior for  $\phi$  is naturally infeasible. As a result, we choose a discrete uniform prior for  $\phi$  in Section 3.1 along with a motivation of keeping  $n_\phi$  moderate yet exploring as many values of  $\phi$  as possible where the posterior mass is distributed. Finally, we choose the prior  $\phi \sim \text{Discrete-Uniform}\{2.5, 2.75, 3, \dots, 17.5\}$  where  $n_\phi = 61$  elements. The trace plot of  $\phi$  in Figure 5 shows that the choice of our prior is reasonable. While the conditional distribution of  $\lambda_p^*$  in (5) involves  $\Sigma_{pp}^{(\phi)}$  matrices as well, we mainly focus on the marginal distributions of the elements of  $\lambda_p^*$  which involve only the diagonal entries of  $\Sigma_{pp}^{(\phi)}$  and they are equal to one. Hence, we never calculate the  $786,702 \times 786,702$ -dimensional  $\Sigma_{pp}^{(\phi)}$  matrices, which is neither computationally feasible nor in terms of storage.

Due to our non-homogeneous Poisson process assumption in Section 3.1, the population values at both the ward and pixel levels are count data that follow a Poisson distribution.

Consequently, the likelihood for  $\lambda_i^*$ 's is non-Gaussian. Given that each ward comprises a large number of pixels and the total population count of a ward is the sum of the pixel-level population sizes, the sampling distribution of the maximum likelihood estimator of  $\lambda_i^*$ , i.e.,  $\hat{\lambda}_i^* (= \log(Y_i/|\mathcal{A}_i|))$  would be approximately normal, by employing the Lindeberg-Feller Central Limit Theorem. This basically provides the Laplace approximation that allows us to handle the non-Gaussian likelihood effectively. Consequently,  $\hat{\lambda}_i^*$  follows a (approximately) normal distribution with mean  $\lambda_i^*$  and variance  $I(\hat{\lambda}_i^*)^{-1}$ . Here,  $I(\hat{\lambda}_i^*) = Y_i$ , thus yielding:

$$L(\lambda_i^*) \propto \exp \left[ -\frac{1}{2} \left( \lambda_i^* - \hat{\lambda}_i^* \right)^2 Y_i \right]. \quad (8)$$

Here,  $\hat{\lambda}_i^*$ 's are empirical log-intensities shown in the right panel of Figure 1. Denoting the vector of ward-wise population sizes by  $\mathbf{Y} = (Y_1, \dots, Y_L)'$ , the vector of empirical log-intensities by  $\hat{\boldsymbol{\lambda}} = (\hat{\lambda}_1^*, \dots, \hat{\lambda}_L^*)$ , and a diagonal matrix with its diagonal elements equal to  $Y_i^{-1}, i = 1, \dots, L$  by  $\text{diag}(\mathbf{1}/\mathbf{Y})$ , we write  $\hat{\boldsymbol{\lambda}}|\boldsymbol{\lambda} \sim N_L(\boldsymbol{\lambda}, \text{diag}(\mathbf{1}/\mathbf{Y}))$ . We later use the notation  $\text{diag}(\mathbf{Y})$  to denote a diagonal matrix with its diagonal elements equal to  $Y_i, i = 1, \dots, L$ . As a result of the above Laplace approximation, the first layer of the Bayesian hierarchical model in (6), i.e.,  $Y_i|\lambda_i^* \stackrel{\text{Indep}}{\sim} \text{Poisson}(|\mathcal{A}_i| \exp\{\lambda_i^*\})$  can be replaced with  $\hat{\boldsymbol{\lambda}}|\boldsymbol{\lambda} \sim N_L(\boldsymbol{\lambda}, \text{diag}(\mathbf{1}/\mathbf{Y}))$ . The idea of replacing the non-Gaussian likelihood in a hierarchical Bayesian model with a Gaussian likelihood based on maximum likelihood and further performing Markov chain Monte Carlo (MCMC) or Integrated Nested Laplace Approximation (INLA) to smooth the underlying latent Gaussian process specification of the spatially-varying parameters have been explored in the literature and called a ‘max-and-smooth’ approach (Hrafinkelsson et al., 2021). This Gaussian approximation of the likelihood allows us to circumvent Metropolis-Hastings sampling, enabling us to proceed with the Gibbs sampling (Gelfand, 2000) while maintaining conjugacy.

In Gibbs sampling with Laplace approximation, we need to draw samples from the posterior  $\pi(\boldsymbol{\lambda}^*, \boldsymbol{\lambda}_p^*, \boldsymbol{\beta}, \sigma^2, \phi|\hat{\boldsymbol{\lambda}}^*) = \pi(\boldsymbol{\lambda}_p^*|\boldsymbol{\lambda}^*, \boldsymbol{\beta}, \sigma^2, \phi, \hat{\boldsymbol{\lambda}}^*) \times \pi(\boldsymbol{\lambda}^*, \boldsymbol{\beta}, \sigma^2, \phi|\hat{\boldsymbol{\lambda}}^*)$ . The first term on the right side does not depend on  $\hat{\boldsymbol{\lambda}}^*$  and is given by (5). We thus focus on drawing samples from  $\pi(\boldsymbol{\lambda}^*, \boldsymbol{\beta}, \sigma^2, \phi|\hat{\boldsymbol{\lambda}}^*)$ . Here, in a Gibbs sampling framework, we draw samples from  $\pi(\boldsymbol{\lambda}^*|\boldsymbol{\beta}, \sigma^2, \phi, \hat{\boldsymbol{\lambda}}^*)$ ,  $\pi(\boldsymbol{\beta}|\boldsymbol{\lambda}^*, \sigma^2, \phi, \hat{\boldsymbol{\lambda}}^*)$ ,  $\pi(\sigma^2|\boldsymbol{\lambda}^*, \boldsymbol{\beta}, \phi, \hat{\boldsymbol{\lambda}}^*)$ , and  $\pi(\phi|\boldsymbol{\lambda}^*, \boldsymbol{\beta}, \sigma^2, \hat{\boldsymbol{\lambda}}^*)$ . As  $|\mathcal{A}_i|$  are

known and fixed, given  $\widehat{\boldsymbol{\lambda}}^*$ , we know  $\mathbf{Y}$  and vice versa. The first three full conditional posteriors are given by

$$\begin{aligned}\boldsymbol{\lambda}^*|\boldsymbol{\beta}, \sigma^2, \phi, \widehat{\boldsymbol{\lambda}}^* &\sim \text{N}_L(\boldsymbol{\mu}^*, \boldsymbol{\Sigma}^*), \\ \boldsymbol{\beta}|\boldsymbol{\lambda}^*, \sigma^2, \phi, \widehat{\boldsymbol{\lambda}}^* &\equiv \boldsymbol{\beta}|\boldsymbol{\lambda}^*, \sigma^2, \phi \sim \text{N}_{m+1}(\boldsymbol{\mu}_1, \boldsymbol{\Sigma}_1), \\ \sigma^2|\boldsymbol{\lambda}^*, \boldsymbol{\beta}, \phi, \widehat{\boldsymbol{\lambda}}^* &\equiv \sigma^2|\boldsymbol{\lambda}^*, \boldsymbol{\beta}, \phi \sim \text{Inverse-Gamma}(A, B),\end{aligned}\tag{9}$$

where the expressions for  $\boldsymbol{\mu}^*$ ,  $\boldsymbol{\Sigma}^*$ ,  $\boldsymbol{\mu}_1$ ,  $\boldsymbol{\Sigma}_1$ ,  $A$ , and  $B$  are given by

$$\begin{aligned}\boldsymbol{\Sigma}^* &= \left( \frac{1}{\sigma^2} \boldsymbol{\Sigma}_{00}^{(\phi)-1} + \text{diag}(\mathbf{Y}) \right)^{-1}, \quad \boldsymbol{\mu}^* = \boldsymbol{\Sigma}^* \left( \frac{1}{\sigma^2} \boldsymbol{\Sigma}_{00}^{(\phi)-1} \widetilde{\mathbf{X}} \boldsymbol{\beta} + \text{diag}(\mathbf{Y}) \widehat{\boldsymbol{\lambda}}^* \right), \\ \boldsymbol{\Sigma}_1 &= \left( \frac{1}{\sigma^2} \widetilde{\mathbf{X}}^T \boldsymbol{\Sigma}_{00}^{(\phi)-1} \widetilde{\mathbf{X}} + \frac{1}{100^2} \mathbf{I}_{m+1} \right)^{-1}, \quad \boldsymbol{\mu}_1 = \boldsymbol{\Sigma}_1 \left( \frac{1}{\sigma^2} \widetilde{\mathbf{X}}^T \boldsymbol{\Sigma}_{00}^{(\phi)-1} \boldsymbol{\lambda}^* \right), \\ A &= 0.01 + \frac{L}{2}, \quad B = 0.01 + \frac{1}{2} \left( \boldsymbol{\lambda}^* - \widetilde{\mathbf{X}} \boldsymbol{\beta} \right)^T \boldsymbol{\Sigma}_{00}^{(\phi)-1} \left( \boldsymbol{\lambda}^* - \widetilde{\mathbf{X}} \boldsymbol{\beta} \right).\end{aligned}$$

Further,  $\pi(\phi|\boldsymbol{\lambda}^*, \boldsymbol{\beta}, \sigma^2, \widehat{\boldsymbol{\lambda}}^*)$  is equal to  $\pi(\phi|\boldsymbol{\lambda}^*, \boldsymbol{\beta}, \sigma^2) \propto f_{\text{N}_L}(\boldsymbol{\lambda}^*; \widetilde{\mathbf{X}} \boldsymbol{\beta}, \sigma^2 \boldsymbol{\Sigma}_{00}^{(\phi)})$ , where  $f_{\text{N}_L}(\cdot; \widetilde{\boldsymbol{\mu}}, \widetilde{\boldsymbol{\Sigma}})$  denotes the density of a  $L$ -variate normal distribution with mean vector and covariance matrix given by  $\widetilde{\boldsymbol{\mu}}$  and  $\widetilde{\boldsymbol{\Sigma}}$ , respectively. Thus, we draw samples from  $\pi(\phi|\boldsymbol{\lambda}^*, \boldsymbol{\beta}, \sigma^2)$  using a probability proportional to size (PPS) sampling on values of  $\phi$ , where the weights assigned to the values in the parameter space of  $\phi$  are  $\pi(\phi|\boldsymbol{\lambda}^*, \boldsymbol{\beta}, \sigma^2)$  scaled to ensure they sum to one. Finally, we obtain MCMC chains for the hyperparameters  $\boldsymbol{\lambda}^*$ ,  $\boldsymbol{\beta}$ ,  $\sigma^2$ , and  $\phi$ .

Given that drawing samples from the 786,702-dimensional multivariate normal distribution  $\pi(\boldsymbol{\lambda}_p^*|\boldsymbol{\lambda}^*, \boldsymbol{\beta}, \sigma^2, \phi, \widehat{\boldsymbol{\lambda}}^*)$  is an infeasible problem, we focus on obtaining the quantities  $\text{E}(\boldsymbol{\lambda}_p^*|\mathbf{Y})$  and the vector of marginal posterior standard deviations  $\text{SD}(\boldsymbol{\lambda}_p^*|\mathbf{Y})$  which are essential. To achieve this, we employ the concepts of conditional mean and conditional covariance to derive the mean and standard deviation from the posterior predictive distribution, as outlined below:

$$\begin{aligned}\text{E}(\boldsymbol{\lambda}_p^*|\mathbf{Y}) &= \text{E} \left[ \text{E}(\boldsymbol{\lambda}_p^*|\boldsymbol{\lambda}^*, \boldsymbol{\beta}, \sigma^2, \phi, \mathbf{Y}) | \mathbf{Y} \right] \\ &= \text{E} \left[ \mathbf{X} \boldsymbol{\beta} + \boldsymbol{\Sigma}_{p0}^{(\phi)} \boldsymbol{\Sigma}_{00}^{(\phi)-1} \left( \boldsymbol{\lambda}^* - \widetilde{\mathbf{X}} \boldsymbol{\beta} \right) | \mathbf{Y} \right] \\ &\approx \frac{1}{B} \sum_{b=1}^B \left[ \mathbf{X} \boldsymbol{\beta}^{(b)} + \boldsymbol{\Sigma}_{p0}^{(\phi^{(b)})} \boldsymbol{\Sigma}_{00}^{(\phi^{(b)})-1} \left( \boldsymbol{\lambda}^{*(b)} - \widetilde{\mathbf{X}} \boldsymbol{\beta}^{(b)} \right) \right].\end{aligned}\tag{10}$$

$$\begin{aligned}
\text{Cov}(\boldsymbol{\lambda}_p^*|\mathbf{Y}) &= \text{E} [\text{Cov}(\boldsymbol{\lambda}_p^*|\boldsymbol{\lambda}^*, \boldsymbol{\beta}, \sigma^2, \phi, \mathbf{Y})|\mathbf{Y}] + \text{Cov} [\text{E}(\boldsymbol{\lambda}_p^*|\boldsymbol{\lambda}^*, \boldsymbol{\beta}, \sigma^2, \phi, \mathbf{Y})|\mathbf{Y}] \\
&= \text{E} \left[ \sigma^2 \left( \boldsymbol{\Sigma}_{pp}^{(\phi)} - \boldsymbol{\Sigma}_{p0}^{(\phi)} \boldsymbol{\Sigma}_{00}^{(\phi)-1} \boldsymbol{\Sigma}_{0p}^{(\phi)} \right) | \mathbf{Y} \right] \\
&\quad + \text{Cov} \left[ \mathbf{X}\boldsymbol{\beta} + \boldsymbol{\Sigma}_{p0}^{(\phi)} \boldsymbol{\Sigma}_{00}^{(\phi)-1} \left( \boldsymbol{\lambda}^* - \widetilde{\mathbf{X}}\boldsymbol{\beta} \right) | \mathbf{Y} \right] \\
&\approx \frac{1}{B} \sum_{i=1}^B \left[ \sigma^{2(b)} \left( \boldsymbol{\Sigma}_{pp}^{(\phi^{(b)})} - \boldsymbol{\Sigma}_{p0}^{(\phi^{(b)})} \boldsymbol{\Sigma}_{00}^{(\phi^{(b)})-1} \boldsymbol{\Sigma}_{0p}^{(\phi^{(b)})} \right) | \mathbf{Y} \right] \\
&\quad + \text{Sample Cov} \left[ \left\{ \mathbf{X}\boldsymbol{\beta}^{(b)} + \boldsymbol{\Sigma}_{p0}^{(\phi^{(b)})} \boldsymbol{\Sigma}_{00}^{(\phi^{(b)})-1} \left( \boldsymbol{\lambda}^{*(b)} - \widetilde{\mathbf{X}}\boldsymbol{\beta}^{(b)} \right) \right\}_{b=1}^B \right]. \quad (11)
\end{aligned}$$

While computing the terms like  $\mathbf{X}\boldsymbol{\beta}^{(b)}$ , it is advisable not to form matrices of dimension  $786,702 \times B$  where  $B$  is large in general; for our application, we have  $B = 1500$  and the storage cost of a  $786,702 \times 1500$ -dimensional matrix is approximately 9 GB making the computation vulnerable on a standard desktop. We divide the computation into different wards and calculate such terms for one ward at a time. Besides, we focus only on the diagonal elements of  $\text{Cov}(\boldsymbol{\lambda}_p^*|\mathbf{Y})$ , which involves the diagonal elements of  $\boldsymbol{\Sigma}_{pp}^{(\phi^{(b)})}$  only and they are ones.

## 4 Simulation Study

The purpose of this simulation study is to compare and contrast the proposed model with a standard parametric Bayesian generalized linear model that does not incorporate a Laplace approximation, a parametric Bayesian multiple linear regression model that incorporates a Laplace approximation, and a semiparametric Bayesian model that incorporates a Laplace approximation but replaces the dense Gaussian process prior for the intensity function with spatially-independent white noise. The covariates used in the study are the same as they are in the setup of the problem statement. We simulate data under three different situations as follows. Here each setting aims to assess the performance and robustness of the proposed model against existing and simpler models under varying degrees of spatial smoothness of the intensity function and its tiny (the coefficients of the sine and cosine terms are only 0.05 and

0.1) deviation from a linear combination of the available predictor surfaces.

$$\text{S1 : } \log[\lambda(\mathbf{s})] = \mathbf{X}(\mathbf{s})^T \boldsymbol{\beta}$$

$$\text{S2 : } \log[\lambda(\mathbf{s})] = \mathbf{X}(\mathbf{s})^T \boldsymbol{\beta} + 0.05 \sin(2\pi s_1^*) + 0.05 \cos(2\pi s_2^*)$$

$$\text{S3 : } \log[\lambda(\mathbf{s})] = \mathbf{X}(\mathbf{s})^T \boldsymbol{\beta} + 0.1 \sin(2\pi s_1^*) + 0.1 \cos(2\pi s_2^*)$$

Here,  $\mathbf{X}(\mathbf{s})$  represents the predictor vector at location  $\mathbf{s}$ , and  $s_1^*$  and  $s_2^*$  are respectively the scaled row number and scaled column number of the pixel under consideration (scaled row/column number implies row/column number divided by the maximum row/column number). In all settings, the values assigned to  $\boldsymbol{\beta}$  are the least squares estimates obtained from a simple linear regression run on the empirical log-intensity and predictors described in Section 2. The smooth curve concatenated to the linear predictor in settings S2 and S3 adds a surface to the data that deviates from the plane spanned by  $\mathbf{X}(\mathbf{s})^T \boldsymbol{\beta}$  and smooth and nonlinear to any predictor (sinusoidal) in nature. Suppose we call the true value of the vector  $\boldsymbol{\lambda}_p^*$ , obtained according to settings S1, S2, and S3, using a generic notation  $\boldsymbol{\lambda}_p^{*(true)}$ .

For each of the given settings, we analyze the results based on four different models. The first model (BayesGLM) is the Bayesian Generalized Linear Model, fit using `bayesglm` in R. The other models use the Laplace Approximation, approximating the Poisson likelihood with a Gaussian distribution. In the second model (Laplace),  $\eta(\mathbf{s})$  in (2) is set to 0, implying no effect of the smooth term in the model. The third model (Laplace-WN) assumes that  $\eta(\cdot)$  follows a Gaussian white noise process, i.e.,  $\eta(\mathbf{s}) \stackrel{\text{IID}}{\sim} \text{Normal}(0, \sigma^2)$ . The final model (Laplace-GP), formulated in this paper, assumes that  $\eta(\cdot)$  follows a Gaussian process with an exponential covariance kernel.

For each model in each setting, we report a range of statistical measures, including root mean squared error (RMSE), mean absolute deviation (MAD), average posterior standard deviation (PosSD), empirical coverage (Cover), deviance information criterion (DIC), Watanabe-Akaike information criterion (WAIC), and the computation time (in seconds). Here, RMSE and MAD denote the  $L_2$  and  $L_1$  distances between the posterior mean of  $\boldsymbol{\lambda}_p^*$  and  $\boldsymbol{\lambda}_p^{*(true)}$ , respec-



tively. Further, PosSD denotes the average of the elementwise posterior standard deviations of  $\lambda_p^*$ . The measure Cover denotes the coverage of the 95% pointwise normal approximated posterior credible regions of  $\lambda_p^*$  obtained using the element-wise posterior means and posterior standard deviations and then averaging out across the pixels. DIC and WAIC are standard measures for comparing Bayesian models. We simulate 100 datasets from each setting and fit all the four competing models and report the averages of the above-mentioned measures in Table 2. Furthermore, in the simulation study, we consider a single value of  $\phi = 10$  for the model Laplace-GP wherever necessary to allow feasible computation on a standard desktop. This simplification is essential given the complexity of the entire computation process, which is constrained by both space and time limitations.

Table 2: Results of the simulation study for three data generation settings (S1, S2, and S3) and four models for each setting. We report the RMSE, MAD, posterior standard deviation, Empirical Coverage, DIC, WAIC, and computation time (in seconds). A model with smaller RMSE, MAD, PosSD, DIC, WAIC, and computation time and higher Cover is preferred.

Setting	Model	RMSE	MAD	PosSD	Cover	DIC	WAIC	Time(s)
S1	BayesGLM	0.006	0.005	0.006	0.961	6658.068	2686.272	38.227
	Laplace	0.006	0.005	0.006	0.961	6658.014	2686.204	0.414
	Laplace-WN	0.007	0.005	0.079	1.000	6597.706	2699.187	48.333
	Laplace-GP	0.008	0.006	0.020	1.000	6498.361	2738.884	208.213
S2	BayesGLM	0.074	0.059	0.006	0.120	42015.896	19061.157	38.198
	Laplace	0.074	0.059	0.006	0.119	42035.586	19070.840	0.400
	Laplace-WN	0.151	0.113	2.943	1.000	6563.456	2867.129	47.802
	Laplace-GP	0.085	0.065	0.133	1.000	6560.979	2863.246	205.803
S3	BayesGLM	0.148	0.117	0.006	0.060	145714.742	67067.684	37.506
	Laplace	0.148	0.117	0.006	0.060	146017.145	67237.061	0.397
	Laplace-WN	0.305	0.229	5.938	1.000	6552.044	2859.617	46.714
	Laplace-GP	0.171	0.132	0.265	1.000	6551.136	2858.162	202.824

For all settings, the Laplace model has the least computation time, while our Laplace-GP model requires the most computation time; however, obtaining posterior estimates along with uncertainty measures for a 786,702-dimensional parameter vector in approximately 200 seconds is reasonable (apart from pre-calculated  $\Sigma_{00}^{(\phi)}$  and  $\Sigma_{p0}^{(\phi)}$  matrices). RMSE and MAD values do not vary significantly, so no model is consistently preferred based on these measures,

although the Laplace-WN model performs slightly poorer in settings S2 and S3. The Laplace-WN and Laplace-GP models demonstrate significantly better empirical coverage than the others across all settings, particularly in S2 and S3, where there exists a smooth surface in the data generating mechanism. For S1, DIC and WAIC values are almost similar across the different models. However, in S2 and S3, the Laplace-GP model is favored, as it has the lowest DIC and WAIC values—slightly lower than those of the Laplace-WN model and significantly lower than those of the BayesGLM or Laplace models. The debate remains over whether to choose the Laplace-WN or Laplace-GP model for modeling our data. This decision is guided by PosSD, which is significantly lower for the Laplace-GP model compared to the Laplace-WN model. Therefore, we prefer the Laplace-GP model after considering several measures for model comparison. Additionally, the choice of the Laplace-GP model is justified for our data as it exhibits significant spatial smoothness, as shown in the variogram study in Figure 4.

## 5 Data application

We apply our proposed methodology and computation scheme for the dataset described in Section 2. To draw posterior inferences according to Section 3.3, we run the MCMC chain for the hyperparameters  $(\beta, \sigma^2, \phi)$  and the parameters  $(\lambda^*)$ . The process is carried out with 500 burn-in samples and 1500 posterior samples. The trace plots of the MCMC chains for all hyperparameters are illustrated using trace plots in Figure 5. We also show the trace plots of the 50-th and 100-th (arbitrarily chosen) elements of  $\lambda^*$ . These plots demonstrate reasonable mixing and convergence of the MCMC chains for all parameters and hyperparameters. Furthermore, we observe that the chains exhibit fast convergence for all the hyperparameters and parameters. For  $\lambda^*$ , the initial value is chosen as the vector of empirical log-intensities  $\hat{\lambda}^*$ . Further, we regress  $\hat{\lambda}^*$  on  $\widetilde{\mathbf{X}}$  in a simple linear regression format and start the chains of  $\beta$  and  $\sigma^2$  from the estimated regression coefficients and the average of the squared residuals. Given the reasonable quality of the MCMC chains, it is valid to proceed with posterior inferences based on these samples.

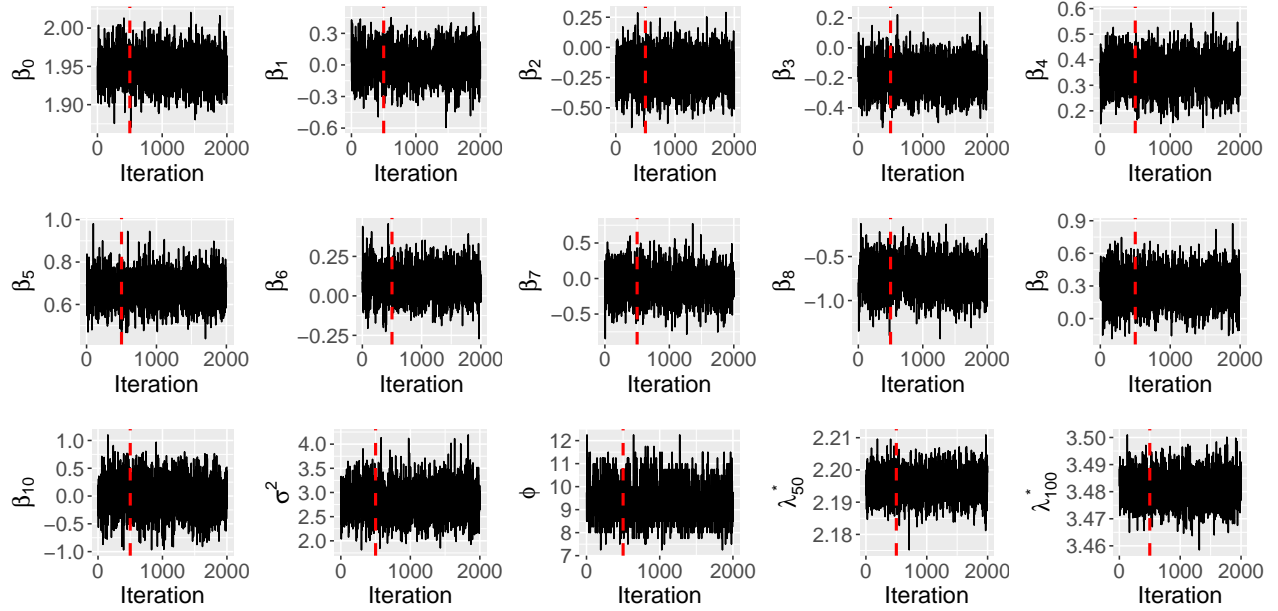


Figure 5: Trace plots for the model hyperparameters  $\beta$ 's,  $\sigma^2$ , and  $\phi$ , and also for  $\lambda_{50}^*$  and  $\lambda_{100}^*$ . Here, the burn-in size is 500, indicated by the red vertical lines.

Table 3 presents the posterior inference for the hyperparameters. The posterior means of the elements of  $\beta$  are positive for Land cover-Vegetation, Land cover-Vacant, Builtup Count, and Vegetation count; except for Builtup Count, a negative posterior mean for the other three is reasonable as the population density is likely to be less in areas with vegetation. Considering Builtup Count, the 95% posterior credible interval includes zero indicating that the corresponding coefficient is not significantly negative, which is reasonable. A parametric Bayesian generalized linear model (`bayesglm`) provides a significant negative effect of Builtup Count in Table 1, which is counter-intuitive. Unlike `bayesglm`, the 95% credible intervals based on the proposed semiparametric Bayesian spatial model include zero for several elements of  $\beta$  correctly identifying the significantly linearly-related predictors.

Figure 6 illustrates the posterior mean and standard deviation for the parameter  $\lambda^*$  that we map onto the actual outline of Bangalore. Higher values of the posterior mean are observed in the center of the city compared to the outskirts. This indicates that ward-level population densities are actually higher in the central areas of Bangalore than in the wards far from the center. The posterior standard deviation is small throughout the city, although the central

Table 3: Posterior means, standard deviations (SD), and equal-tailed 95% credible intervals of the model hyperparameters. The names of predictors corresponding to  $\beta$ 's are provided within brackets in the first column.

Parameter	Posterior Mean	Posterior SD	Credible Interval
$\beta_0$ (Intercept)	1.9469	0.0212	(1.9049, 1.9882)
$\beta_1$ (Land cover-Vegetation)	0.0082	0.1480	(-0.2770, 0.3055)
$\beta_2$ (Land cover-Water)	-0.1970	0.1449	(-0.4830, 0.0788)
$\beta_3$ (Land cover-Vacant)	-0.1918	0.1061	(-0.3953, 0.0179)
$\beta_4$ (Land Use)	0.3431	0.0681	(0.2074, 0.4758)
$\beta_5$ (Street Density)	0.6730	0.0737	(0.5337, 0.8164)
$\beta_6$ (Building Height)	0.0861	0.0931	(-0.0943, 0.2684)
$\beta_7$ (Builtup Count)	-0.0872	0.2086	(-0.4968, 0.3193)
$\beta_8$ (Vegetation Count)	-0.7476	0.1846	(-1.0986, -0.3691)
$\beta_9$ (Vacant Count)	0.2812	0.1534	(-0.0124, 0.5851)
$\beta_{10}$ (Drainage Density)	0.0068	0.3139	(-0.6262, 0.6232)
$\sigma^2$	2.7865	0.3566	(2.1562, 3.5380)
$\phi$	9.2992	0.7863	(8, 11)

areas exhibit slightly higher variability in the estimates than the peripheral wards. Further, it is observed that the estimated intensities closely mirror the empirical intensities, hinting that the max-and-smooth approach in Section 3.3 provides limited spatial smoothness in the posterior distribution of  $\lambda^*$  but does not change abruptly, which is reasonable.

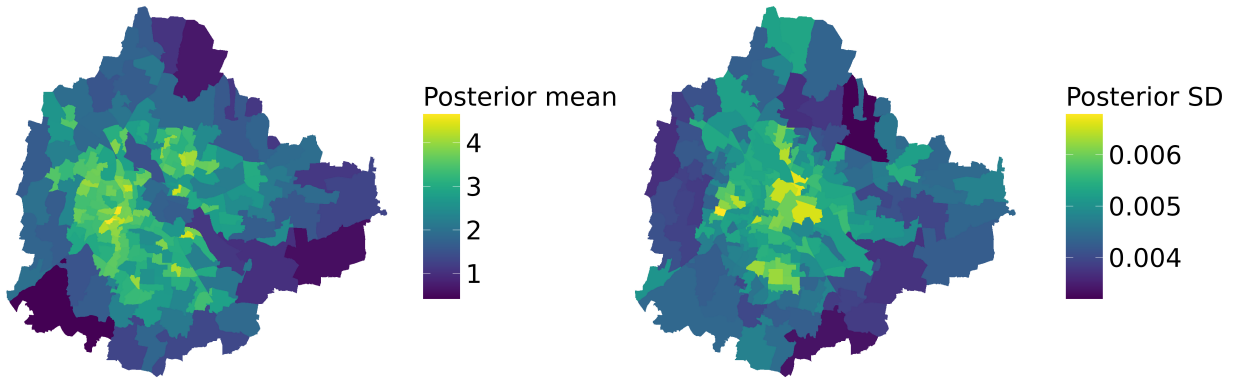


Figure 6: Left: Ward-level posterior means of  $\lambda_i^*$ 's, Right: Ward-level posterior standard deviations for  $\lambda_i^*$ 's.

In the final stage of computation, our goal is to obtain inference about the marginal posterior means and standard deviations of the elements of  $\boldsymbol{\lambda}_p^*$ . These rates provide important

insights into the density of the population at a much higher resolution (here,  $30\text{m} \times 30\text{m}$ ) compared to the ward-level data we have. Hence, the problem of spatial downscaling has been addressed, and we now have the rates at the pixel level, which can be used for redefining boundaries of wards and provide important ideas about social and ecological aspects like water distribution networks. Figure 7 gives us a summary of the above, where we can see the spatial variability of the disaggregated population density estimates (in log scale), along with the underlying uncertainty estimates, across the city. Overall, the map structure shows some similarity to the ward-level maps, in the sense that the wards with higher intensities also have pixels with higher intensities, as we observe the yellow regions towards the center. The standard deviation map does not show much variation, with the exception of several blue dots in the central region. These hint at lower variability due to smaller ward definitions towards the center, leading to more precise posterior inferences near the center.

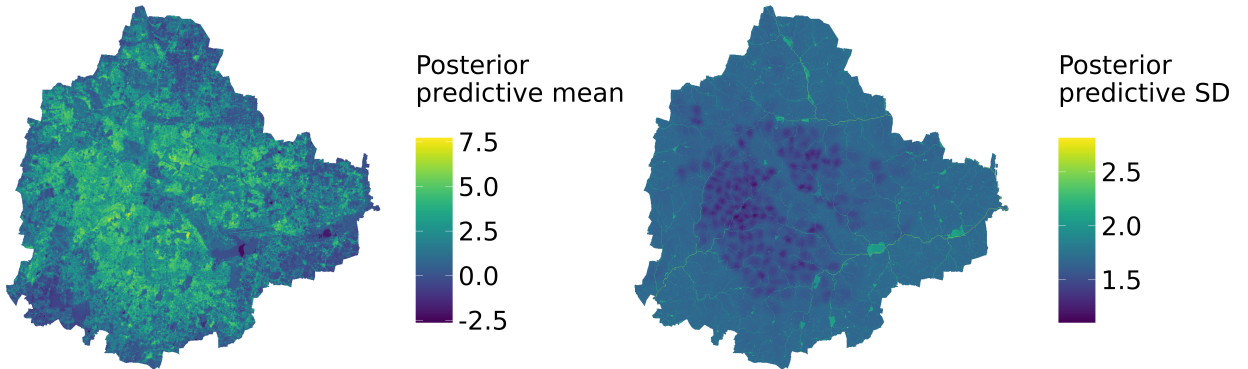


Figure 7: Left: Posterior predictive means for  $\lambda_p^*$ , i.e., the disaggregated population density estimates (in log scale). Right: Posterior predictive standard deviation for  $\lambda_p^*$ , providing the uncertainty estimates in estimating disaggregated population densities (in log scale).

## 6 Conclusion

The Census of India provides publicly available datasets at the ward level that are large portions of a metropolitan area, and wards are generally not based on precise information about

public services like water distribution networks. As a result, for public services and several environmental factors, having a precise idea of population density at a finer spatial resolution is necessary. Motivated by this problem, we discuss a semiparametric hierarchical Bayesian latent Gaussian model framework that uses alternative data sources to obtain precise estimates of a high-resolution population density map. While existing literature discusses similar spatial disaggregation problems (Nandi et al., 2023), the implementation assumes model-based approximations of the underlying Gaussian process, using a stochastic partial differential equation, for example (Lindgren et al., 2011). Besides, usual implementations generally do not involve disaggregating the available data into almost a million pixels, with a few exceptions like Utazi et al. (2019). We discuss tricks for computing covariance matrices for the aggregates on a limited computation resource, the max-and-smooth approach of Hrafnkelsson et al. (2021) in our setup, and also how to obtain elementwise posterior means and standard deviations. The simulation study ensures a better performance of the proposed methodology over existing and simplified models.

The results indicate that the significant predictors of population density are the variables: Land Use, Street Density, Vegetation Count, where the last one is negatively related. After considering the effects of all the available predictors, the estimated spatial range ( $3\phi$  for exponential correlation kernel) is approximately 837 meters, which is realistic for fast-developing cities like Bangalore, where sharp spatial variation between rural and urban areas are generally visible due to lower land price of the rural areas compared to the central regions of the city. The Bangalore city often faces a massive water crisis (Naaz, 2024). The impact on the environment can also be assessed at a high spatial resolution based on our findings.

While our methodology is motivated by the Bangalore population dataset, it can be applied to various disaggregation problems in various scientific disciplines. While we explore the Poisson likelihood setup, similar ideas can be used for any general non-Gaussian likelihood. Motivated by the exploratory data analysis, we stick to the exponential covariance; however, other kernels like squared exponential and Matérn can also be used in different setups.

## References

- Alber, A. and Piégay, H. (2011). Spatial disaggregation and aggregation procedures for characterizing fluvial features at the network-scale: Application to the Rhone basin (France). *Geomorphology*, 125(3):343–360.
- Anjoy, P., Chandra, H., and Basak, P. (2019). Estimation of disaggregate-level poverty incidence in Odisha under area-level hierarchical Bayes small area model. *Social Indicators Research*, 144:251–273.
- Arambepola, R., Lucas, T. C., Nandi, A. K., Gething, P. W., and Cameron, E. (2022). A simulation study of disaggregation regression for spatial disease mapping. *Statistics in Medicine*, 41(1):1–16.
- Balakrishnan, K. (2020). A method for urban population density prediction at 30m resolution. *Cartography and Geographic Information Science*, 47(3):193–213.
- Berliner, L. M., Wikle, C. K., and Cressie, N. (2000). Long-lead prediction of Pacific SSTs via Bayesian dynamic modeling. *Journal of climate*, 13(22):3953–3968.
- Brooks, S., Gelman, A., Jones, G., and Meng, X.-L. (2011). *Handbook of Markov chain Monte Carlo*. CRC press, New York.
- Bullock, Z., Zimmaro, P., Lavrentiadis, G., Wang, P., Ojomo, O., Asimaki, D., Rathje, E. M., and Stewart, J. P. (2023). A latent Gaussian process model for the spatial distribution of liquefaction manifestation. *Earthquake Spectra*, 39(2):1189–1213.
- Cisneros, D., Gong, Y., Yadav, R., Hazra, A., and Huser, R. (2023). A combined statistical and machine learning approach for spatial prediction of extreme wildfire frequencies and sizes. *Extremes*, 26(2):301–330.
- de Oliveira, G. A., da Silva Ribeiro, A. A., and Cirilo, J. A. (2023). Collaborative spatial information as an alternative data source for hydrodynamic model calibration: a Pernambuco State case study, Brazil. *Natural Hazards*, pages 1–25.
- Earnest, A., Beard, J. R., Morgan, G., Lincoln, D., Summerhayes, R., Donoghue, D., Dunn, T., Muscatello, D., and Mengersen, K. (2010). Small area estimation of sparse disease counts using shared component models-application to birth defect registry data in New South Wales, Australia. *Health & place*, 16(4):684–693.
- Foulkes, M. and Newbold, K. B. (2008). Using alternative data sources to study rural migration: examples from Illinois. *Population, Space and Place*, 14(3):177–188.
- Gelfand, A. E. (2000). Gibbs sampling. *Journal of the American statistical Association*, 95(452):1300–1304.
- Gelfand, A. E. and Schliep, E. M. (2016). Spatial statistics and gaussian processes: A beautiful marriage. *Spatial Statistics*, pages 86–104.
- Golder, S. A. and Macy, M. W. (2011). Diurnal and seasonal mood vary with work, sleep, and daylength across diverse cultures. *Science*, 333(6051):1878–1881.

- Harva, M. et al. (2008). *Algorithms for approximate Bayesian inference with applications to astronomical data analysis*. Teknillinen korkeakoulu.
- Hazra, A., Huser, R., and Bolin, D. (2021). Realistic and fast modeling of spatial extremes over large geographical domains. *arXiv preprint arXiv:2112.10248*.
- Hazra, A., Huser, R., and Jóhannesson, Á. V. (2023). *Bayesian Latent Gaussian Models for High-Dimensional Spatial Extremes*, pages 219–251. Springer International Publishing, Cham.
- Hrafnkelsson, B. and Bakka, H. (2023). *Bayesian Latent Gaussian Models*, pages 1–80. Springer International Publishing, Cham.
- Hrafnkelsson, B., Siegert, S., Huser, R., Bakka, H., and Jóhannesson, Á. V. (2021). Max-and-Smooth: a two-step approach for approximate Bayesian inference in latent Gaussian models. *Bayesian Analysis*, 16(2):611–638.
- Irekponor, V., Abdul-Rahman, M., Agunbiade, M., and Bustamente, A. (2022). A framework to determine micro-level population figures using spatially disaggregated population estimates. *arXiv preprint arXiv:2212.02020*.
- Jóhannesson, Á. V., Siegert, S., Huser, R., Bakka, H., and Hrafnkelsson, B. (2022). Approximate Bayesian inference for analysis of spatiotemporal flood frequency data. *The Annals of Applied Statistics*, 16(2):905–935.
- Li, C.-H., Mao, J.-J., Wu, Y.-J., Zhang, B., Zhuang, X., Qin, G., and Liu, H.-M. (2023). Combined impacts of environmental and socioeconomic covariates on HFMD risk in China: A spatiotemporal heterogeneous perspective. *PLOS Neglected Tropical Diseases*, 17(5):e0011286.
- Lindgren, F., Rue, H., and Lindström, J. (2011). An explicit link between Gaussian fields and Gaussian Markov random fields: the stochastic partial differential equation approach. *Journal of the Royal Statistical Society Series B: Statistical Methodology*, 73(4):423–498.
- Machado, A. M., Giehl, E. L. H., Fernandes, L. P., Ingram, S. N., and Daura-Jorge, F. G. (2021). Alternative data sources can fill the gaps in data-poor fisheries. *ICES Journal of Marine Science*, 78(5):1663–1671.
- Martino, S., Akerkar, R., and Rue, H. (2011). Approximate Bayesian inference for survival models. *Scandinavian Journal of Statistics*, 38(3):514–528.
- Mertens, B. and Lambin, E. F. (1997). Spatial modelling of deforestation in southern Cameroon: spatial disaggregation of diverse deforestation processes. *Applied Geography*, 17(2):143–162.
- Monteiro, J., Martins, B., Murrieta-Flores, P., and Pires, J. M. (2019). Spatial disaggregation of historical census data leveraging multiple sources of ancillary information. *ISPRS International Journal of Geo-Information*, 8(8).



- Muhling, B. A., Gaitán, C. F., Stock, C. A., Saba, V. S., Tommasi, D., and Dixon, K. W. (2018). Potential salinity and temperature futures for the chesapeake bay using a statistical downscaling spatial disaggregation framework. *Estuaries and Coasts*, 41:349–372.
- Murphy, K. J., Ciuti, S., Burkitt, T., and Morera-Pujol, V. (2023). Bayesian areal disaggregation regression to predict wildlife distribution and relative density with low-resolution data. *Ecological Applications*, 33(8):e2924.
- Naaz, F. (2024). Bengaluru water supply cut alert! bswwb warns of water shortage on these days.
- Nandi, A. K., Lucas, T. C. D., Arambepola, R., Gething, P., and Weiss, D. J. (2023). disaggregation: An R Package for Bayesian Spatial Disaggregation Modeling. *Journal of Statistical Software*, 106(11):1–19.
- Paige, J., Fuglstad, G.-A., Riebler, A., and Wakefield, J. (2022). Spatial aggregation with respect to a population distribution: Impact on inference. *Spatial Statistics*, 52:100714.
- Pollet, T. V., Stulp, G., Henzi, S. P., and Barrett, L. (2015). Taking the aggravation out of data aggregation: A conceptual guide to dealing with statistical issues related to the pooling of individual-level observational data. *American journal of primatology*, 77(7):727–740.
- Ponciano, J. M., Taper, M. L., Dennis, B., and Lele, S. R. (2009). Hierarchical models in ecology: confidence intervals, hypothesis testing, and model selection using data cloning. *Ecology*, 90(2):356–362.
- Roquette, R., Nunes, B., and Painho, M. (2018). The relevance of spatial aggregation level and of applied methods in the analysis of geographical distribution of cancer mortality in mainland Portugal (2009–2013). *Population health metrics*, 16:1–12.
- Rudstrom, M., Popp, M., Manning, P., and Gbur, E. (2002). Data aggregation issues for crop yield risk analysis. *Canadian Journal of Agricultural Economics/Revue canadienne d’agroeconomie*, 50(2):185–200.
- Rue, H., Martino, S., and Chopin, N. (2009). Approximate Bayesian inference for latent Gaussian models by using integrated nested Laplace approximations. *Journal of the Royal Statistical Society Series B: Statistical Methodology*, 71(2):319–392.
- Sadik, K., Anisa, R., and Aqmaliyah, E. (2020). Small Area Estimation on Zero-Inflated Data Using Frequentist and Bayesian Approach. *Journal of Modern Applied Statistical Methods*, 18(1):8.
- Sawicki, D. S. (1973). Studies of aggregated areal data: problems of statistical inference. *Land Economics*, 49(1):109–114.
- Schmid, C. H. and Brown, E. N. (2000). Bayesian hierarchical models. *Methods in enzymology*, 321:305–330.
- Segond, M.-L., Neokleous, N., Makropoulos, C., Onof, C., and Maksimovic, C. (2007). Simulation and spatio-temporal disaggregation of multi-site rainfall data for urban drainage applications. *Hydrological sciences journal*, 52(5):917–935.

- Shiferaw, Y. A. (2023). Mapping Disaggregate-Level Agricultural Households in South Africa Using a Hierarchical Bayes Small Area Estimation Approach. *Agriculture*, 13(3):631.
- Stumpf, M. P. (2014). Approximate Bayesian inference for complex ecosystems. *F1000Prime Reports*, 6.
- Sudhira, H., Ramachandra, T., and Subrahmanya, M. B. (2007). City profile. *Cities*, 24(5):379–390.
- Tapia, G., Elwany, A. H., and Sang, H. (2016). Prediction of porosity in metal-based additive manufacturing using spatial Gaussian process models. *Additive Manufacturing*, 12:282–290.
- Tasic, I., Porter, R. J., and Brewer, S. (2016). Applications of generalized additive and Bayesian hierarchical models for areal safety analysis: case study of an urban multimodal transportation system in Chicago, Illinois. *Transportation research record*, 2601(1):99–109.
- Tassone, E. C., Miranda, M. L., and Gelfand, A. E. (2010). Disaggregated spatial modelling for areal unit categorical data. *Journal of the Royal Statistical Society Series C: Applied Statistics*, 59(1):175–190.
- Utazi, C., Thorley, J., Alegana, V., Ferrari, M., Nilsen, K., Takahashi, S., Metcalf, C. J. E., Lessler, J., and Tatem, A. (2019). A spatial regression model for the disaggregation of areal unit based data to high-resolution grids with application to vaccination coverage mapping. *Statistical Methods in Medical Research*, 28(10-11):3226–3241.
- van Beurden, A. U. and Douven, W. J. (1999). Aggregation issues of spatial information in environmental research. *International Journal of Geographical Information Science*, 13(5):513–527.
- Wainwright, H. M., Flores Orozco, A., Bucker, M., Dafflon, B., Chen, J., Hubbard, S. S., and Williams, K. H. (2016). Hierarchical Bayesian method for mapping biogeochemical hot spots using induced polarization imaging. *Water Resources Research*, 52(1):533–551.
- Wikle, C. K. (2003). Hierarchical bayesian models for predicting the spread of ecological processes. *Ecology*, 84(6):1382–1394.
- Wulder, M. A., Masek, J. G., et al. (2012). Landsat legacy. *Remote Sensing of Environment*, 122:1–202.
- Yadav, R., Huser, R., Opitz, T., and Lombardo, L. (2023). Joint modelling of landslide counts and sizes using spatial marked point processes with sub-asymptotic mark distributions. *Journal of the Royal Statistical Society Series C: Applied Statistics*, 72(5):1139–1161.
- Yang, Y., Gao, H., Berry, C., Carrick, D., Radjenovic, A., and Husmeier, D. (2022). Classification of myocardial blood flow based on dynamic contrast-enhanced magnetic resonance imaging using hierarchical Bayesian models. *Journal of the Royal Statistical Society Series C: Applied Statistics*, 71(5):1085–1115.
- You, L., Wood, S., and Wood-Sichra, U. (2009). Generating plausible crop distribution maps for Sub-Saharan Africa using a spatially disaggregated data fusion and optimization approach. *Agricultural Systems*, 99(2-3):126–140.